ORIGINAL PAPER

CrossMark

Functionalized graphene–polyaniline nanocomposite as electrode material for asymmetric supercapacitors

Changyuan Bao[1] · Qingqing He[2] · Jiajun Han[1] · Jinning Cheng[1] · Ruitao Zhang[1]

Abstract

A polyaniline/sulfonated graphene (PANI/SG) nanostructure was synthesized as electrode material for an asymmetric supercapacitor via a novel in situ chemical oxidative polymerization method including two oxidants. The composite's structure and morphology were characterized by Fourier-transform infrared spectroscopy (FTIR), X-ray diffraction (XRD), X-ray photo-electron spectroscopy (XPS), field-emission scanning electron microscopy (FESEM), and transmission electron microscopy (TEM) measurements. Furthermore, the electrochemical performances of the composite were characterized by cyclic voltammetry (CV), galvanostatic charge–discharge (GCD), and electrochemical impedance spectroscopy (EIS) techniques in detail. In addition, we have triumphantly manufactured an asymmetric supercapacitor (ASC) employing activated carbon (AC) and PANI/SG as the positive and negative electrodes, respectively. The ASC possessed an extended potential window (1.4 V), a remarkable cycling property (85.9% capacitance retention after 5000 cycles), and a satisfactory average energy and power density (23 Wh/kg and 6.1 kW/kg).

Introduction

Since the end of the last century, unprecedented energy consumption and global climate changes are two major problems which the world are facing nowadays [1–3]. At present, fossil fuels are still the most mainstream energy resource, whereas with the conspicuous increasing of energy demands, nonrenewable fossil energy will ultimately tend to dry up. The development and use of recyclable energy are the key to solving the problem as we mentioned above [4–7]. Thus, supercapacitors (SCs) have attracted more and more attentions as sustainable green energy generation/storage system suitable for a wide variety of new technological energy applications due to their high power density, rapid charging time, lightweight, long cycle life, and eco-friendly features [8–11]. According to energy storage mechanisms, they categorize in two groups including double electric layer capacitors (DELCs) and pseudocapacitors [12, 13]. The utilization of a

high-activity electrode material is an essential factor for an effective development of a high-property supercapacitor [14, 15].

Recently, various novel electrode materials such as carbon materials (e.g., graphene, carbon nanotubes), conducting polymers (including polyaniline (PANI), polythiophene, and polypyrrole), and transition metal oxides (including Co_3O_4, Mn_2O_3, NiO, RuO_2, etc.) are eagerly pursued in order to achieve better performance [16–20]. In general, electronically conductive polymers utilize redox faradaic reaction to store electric energy and release it, and carbonaceous materials provide a good electron-transfer path for moving the generated energy [21–23]. Thereinto, polyaniline is a promising candidate of low-cost electrode materials for supercapacitor due to its ease of synthesis, high electrical conductivity, good flexibility, and environmental stability [24–29]. However, pure polyaniline usually suffers from strong agglomeration and extremely distortion of its conformation, which lead to a low specific surface area, a weak intercalation or doping for ions, and a poor cycle life [30, 31]. This illustrates single electrode material does not meet all the requirements of supercapacitors. Carbonaceous materials such as graphene and activated carbon are common building blocks for polyaniline nanocomposites [32]. The combination of PANI and graphene may present a rational candidate for the supercapacitor electrode, which has been researching at present. Polyaniline/graphene

✉ Jiajun Han
hanjiajunhitweihai@163.com

1 Department of Applied Chemistry, Harbin Institute of Technology, Weihai 264209, China

2 Department of Chemistry, Zhejiang University, Zhejiang 310058, China

nanocomposite can greatly circumvent the phenomenon of aggregation on account of the great specific surface area of graphene; furthermore, its adsorption effect is outstanding and the presence of RGO provides high surface are for the polymerization of PANI [33]. This facilitates the formation of tightly structured composite materials. We believe that PANI/RGO nanocomposite will give remarkable performance due to combined impact of the layer construction of RGO which facilitate insertion-deinsertion of electrolyte ion and fast kinetics of electrolyte ion migration between the electrode and electrolyte during charge–discharge processes. Furthermore, noteworthy upgrades in their properties can be accomplished because of the collaborative influence between the two components [34]. However, the water solubility of graphene is poor and RGOs easily tend to be irreversibly agglomerative [35]. To address the above issue, the functionalizations of graphene are of crucial importance. PANI arrays on grafted reduced graphene oxide nanostructures are expected to produce uniform structures with higher electrochemical utilization of polyaniline by providing large interaction area between the active materials and electrolyte [36].

Indeed, few previous studies reported performance of sulfonated graphene/PANI materials which were prepared via liquid/liquid interfacial polymerization or LBL self-assembled [37]. In this paper, we prepared the PANI-sulfonated graphene nanocomposite (PANI/SG) as the anode of the supercapacitor through in situ chemical oxidative polymerization. The crystal structure, morphology, and electrochemical performance of PANI/SG nanocomposite were investigated in detail. We also have investigated the electrochemical performance of a PANI-based asymmetric supercapacitor by means of a two-electrode configuration. As a result, studies have shown that electrochemical performances were noticeably improved compared to those of the neat PANI, PANI/GO, and PANI/RGO composites. Obtained results are presented and will be discussed here.

Experimental

Chemicals and materials

Aniline (AN), ammonium persulfate (APS), HCl (37%), H_2SO_4 (98%), $NH_3 \cdot H_2O$ (28%), graphite, $NaNO_3$, $KMnO_4$, H_2O_2, $MnSO_4$, $NaBH_4$, $N_2H_4 \cdot H_2O$ (80%), sulfanilic acid, and anhydrous alcohol are all analytical grade chemicals and purchased from the National Pharmaceutical Group Chemical Reagent Company, No. 52 Ningbo Road, Shanghai, China. Acetylene black is battery grade, purchased from Aladdin, Y891 (Branch), Fengxian District, Shanghai, China. The CR2025-type coin cells and styrene-butadiene rubber (SBR,

40%) are also battery grade, and they are supplied by Shanxi LIZHIYUAN battery materials Co. Ltd., Shanxi, China.

Synthesis of PANI/SG

Preparation of SG

GO was prepared by the reported modified Hummers method [38, 39]. Five hundred milligrams of GO was dispersed in 500 ml of deionized water. Then, 5 g of $NaBH_4$ was added successively and the mixture was heated at 80 °C for 1 h. After being filtered and washed with deionized water over and over again, the solid was redispersed in 500 ml of deionized water and was mildly sonicated. 2.7 g of aryl diazonium salt of sulfanilic acid was added into the redispersion of the partially reduced GO with continuous stirring for 4 h at 0 °C. Next, the mixture was treated by suction filtration and washing. Then, 2 ml of hydrazine hydrate was added successively and the mixture was heated at 95 °C for 2 h. Lastly, the final SG was obtained by centrifugal separation, washed by water for many times, and dried at room temperature for 24 h.

Preparation of PANI/SG composites

PANI/SG nanocomposite was facilely prepared by the in situ polymerization of aniline monomer in the presence of SG. MnO_2 possesses relatively weak oxidizing capacity, which served as a primary oxidizer. The active MnO_2 was prepared according to Ref. [30]. While APS was used as a main oxidant to realize the oxidation of aniline. The typical polymerization procedure is as follows: first, reaction was proceeded in a 1000-ml reaction vessel, and 1.4 g of SG was added into 100 ml of water and sonicated for 30 min at least. Then, 150 g of HCl and 0.5 g of Triton X-100 were successively added into the above mixture and stirred for 1 h. Next, 100 g of deionized ice was added into the reactor to lower temperature below 10 °C. In addition, the mixture was cooled by constant stirring in an ice bath with a temperature of 4–6 °C after the reactive monomer, 70 g of aniline was added to the reactor. Then, as-prepared initiator MnO_2 was added slowly into the well-stirred suspension for 5 to 10 min. Then, after 30 min, 2 g of APS per minute was added to the reactor, repeating 100 times and the temperature should stay below 5 °C simultaneously. The polymerization was undergone at 5–8 °C by adding the ice for 4 h. The resultant mixture was filtered and washed with distilled water for three times and ethanol for one time, and then further dried under vacuum at 60 °C for 1 day to obtain the PANI/SG. Add the appropriate amount of ammonia and hydrazine hydrate to some of the wet powder to remove doping and reduce, and the reduced PANI/SG composite was obtained.

In order to compare the differences of the electrochemical properties with PANI/GO, PANI/RGO, and pure PANI, the

above materials were also prepared by above-mentioned similar procedures excluding some preparation steps.

Structure and morphology characterization

The XRD spectra were recorded on a D/X 2700 diffractometer (Dandong Hao Yuan Instrument Co., Ltd., China) with Cu Kα radiation. XPS measurements were performed on an ESCALAB 250Xi spectrometer (Thermo Fisher Scientific, UK). The morphology and observation were performed on field-emission scanning electron microscopy (MERLIN Compact, Zeiss, Germany) and transmission electron microscope (TEM JEOL-2100, Electronics Co., Ltd., Japan). FTIR spectra were obtained by using a Nicolet 380 FT infrared spectrometer (Us ThermoElectron Corporation, USA) from 4000 to 500 cm^{-1}.

Electrode fabrication and electrochemical measurements

The electrochemical measurements were performed in a three-electrode cell. To evaluate the electrochemical performances of these electrode materials, the working electrodes for supercapacitors were prepared by mixing the active material and styrene-butadiene rubber (SBR) binder in a weight ratio of 19:1. Platinum electrode was used as the counter electrode. The electrolyte was 2 M perchloric acid solution. cyclic voltammetry (CV), electrochemical impedance spectroscopy (EIS), and galvanostatic charge–discharge (GCD) were performed via CHI660E Electrochemical Workstation (CHI660E, Shanghai Chenhua Device Company, China). CV was carried out at a scan rate of 5 mV·s^{-1} between − 0.65 and 0.45 V vs Hg/Hg$_2$SO$_4$. EIS was carried out in the frequency ranging from 0.01 to 100,000 Hz at an open circuit potential with AC voltage amplitude of 5 mV. The GCD curves of these nanocomposites were performed at different current densities between − 0.5 and 0.3 V vs Hg/Hg$_2$SO$_4$.

Moreover, a two-electrode configuration was connected to different electrodes separated by filter paper of the ASC for intact test. The cycle performance of the composites was measured on a LAND-CT2001A cycle life tester (Wuhan Jinnuo Instrument Co. Ltd., Wuhan, China) between − 0.6 and 0.8 V. All measurements were carried out at room temperature.

Assembling of ASC

The neat PANI, PANI/GO, PANI/RGO, and PANI/SG nanocomposites were assembled in a CR2025-type coin cell to investigate their electrochemical performances. The samples were directly compressed on current collectors (stainless steel mesh, 100 meshes, 0.9×0.9 cm) as a working electrode and the treated activated carbon on current collectors as a counter electrode, respectively. The asymmetric supercapacitor was

assembled with a negative electrode, a separator, and a positive electrode. 2 mol/L perchloric acid solution was employed as an electrolyte. The energy density (E, Wh/kg) and power density (P, kW/kg) for ASCs were calculated from the following Eqs. (1) and (2), respectively [40].

$$E = 0.5 \cdot C_m \cdot (\Delta V)^2 / 3.6 \tag{1}$$

$$P = \frac{\left(V_{max} \text{-} V_{drop}\right)^2}{4 R_{ESR} m} \tag{2}$$

$$R_{ESR} = \frac{V_{drop}}{2I} \tag{3}$$

In which, C_m is the specific capacitance (F/g), ΔV is discharge potential range, V_{drop} is the voltage drop at the beginning of the discharge, R_{ESR} is the effective series resistance, I is the applied discharge current (A), and m is the mass of the active materials of the electrode (g).

Results and discussion

Structures and morphologies

According to our previous experience, the use of MnO$_2$ and APS as two oxidants can lead to an increase in the productivity, doping ratio, and conductivity of PANI. To further prove that MnO$_2$ did not remain inside PANI-based materials, XRD and XPS analyses are employed. Figure 1 illustrates XRD patterns of MnO$_2$, SG, PANI, PANI/GO, PANI/RGO, and PANI/SG. The XRD pattern of SG has a broad peak at around $2\theta = 23.9°$, corresponding to the diffraction of the (002) plane derives from sulfonated graphene [36]. For pure MnO$_2$, significant XRD diffraction peaks were recorded at $2\theta = 22.3$, 37.2, and 42.7°, and could be well-assigned to the (120), (131), and (300) planes of γ-MnO$_2$ (JCPDS 14-644), respectively, in good agreement with the literature [41, 42]. For neat PANI, the diffraction peaks appear at $2\theta = 15.2$, 20.6, and 24.4°, corresponding to the (011), (100), and (110) crystal planes of PANI, respectively [43]. These peaks indicated that it was an emeraldine salt. The XRD pattern of the PANI/SG composite has a broad peak at $2\theta = 19.9°$ contributed to the combination of PANI and SG and two smaller diffraction peaks at $2\theta = 24.3$ and 44.4°, which were ascribed to the reflection of SG [44]. Clearly, the peaks located 24.3° appear much sharper, showing superior crystallinity and regularity both contribute significantly to the electrochemical performance of the material. It should be pointed out that there are no characteristic peaks of MnO$_2$ at 2θ of 22.3, 37.2, and 42.7° compared with pure MnO$_2$ because the MnO$_2$ was only a primary oxidant and did not remain in PANI and PANI-based composites.

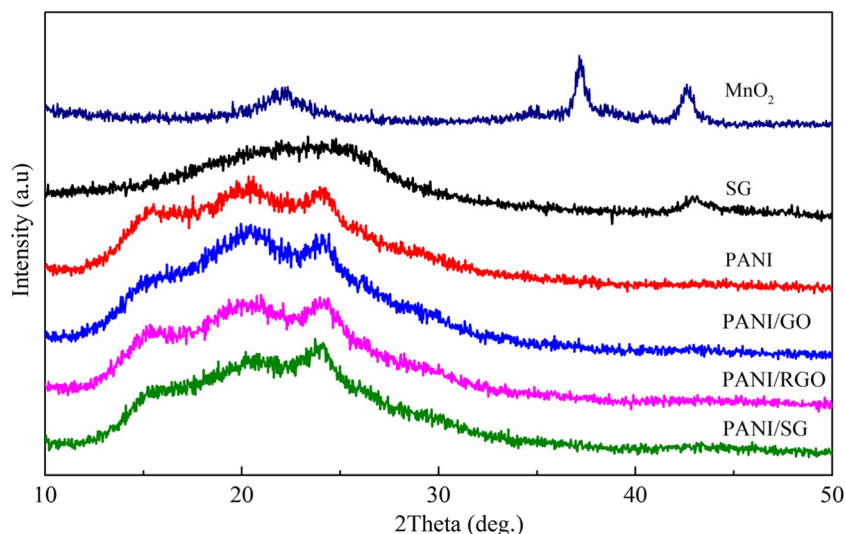**Fig. 1** XRD patterns of MnO$_2$, SG, PANI, PANI/GO, PANI/RGO, and PANI/SG

Figure 2a shows the XPS spectra of PANI/SG composite (all PANI-based composites are prepared by above-mentioned similar procedures). The peaks of O 1 s, N 1 s, and C 1 s can be observed clearly at 530.9, 398.0, and 284.7 eV in the survey spectrum, respectively. Furthermore, the weak S 2p peak centering at 168.2 eV reflects effective introduction of –SO$_3$ on graphene surface in the sample (Fig. 2b). The peak value well agrees with that reported for S element [45]. However, both Mn 2p3/2 peak at 642.1 eV and Mn 2p1/2 peak centering at 653.7 eV are obviously inexistent, which are in good agreement with our assumption that MnO$_2$ ought not to be in the electrode mass [46]. To sum up, XRD and XPS results indicated that there is no MnO$_2$ retaining inside the electrode mass.

Figure 3 represents the FTIR spectra of SG, PANI, PANI/GO, PANI/RGO, and PANI/SG, respectively. The spectrum of the SG confirms the presence of C=C ($\nu_{C=C}$ at 1540 cm^{-1}) and

–SO$_3$H ($\nu_{O=S=O}$ at 1040 cm^{-1} and $\nu_{S-phenyl}$ at 1170 cm^{-1}) [36], indicating the successful sulfonation of graphene. The peak at 870 cm^{-1} is assigned to the characteristic vibrations of a p-disubstituted phenyl group [47]. Absorption bands at 818 cm^{-1} (C–H out of plane bending vibration), 1125 cm^{-1} (N = Q = N, Q denotes quinonoid), 1302 cm^{-1} (C–N stretching vibration), 1490 cm^{-1} (C=C stretching deformation of benzenoid ring), 1565 cm^{-1} (C=C stretching deformation of quinonoid ring), 3030 cm^{-1} (C–H stretching vibration), and 3250 cm^{-1} (N–H stretching vibration) are assigned to PANI specific structure [33]. As similar with primitive polyaniline, the spectrum of PANI-based nanocomposites shows peaks at nearby positions. This confirms that the PANI structures do not change during the addition of other materials into the composites structure. Nevertheless, several peaks shifted to a higher or lower wavenumber on account of the conjugate interaction between PANI chains and graphene substrate.
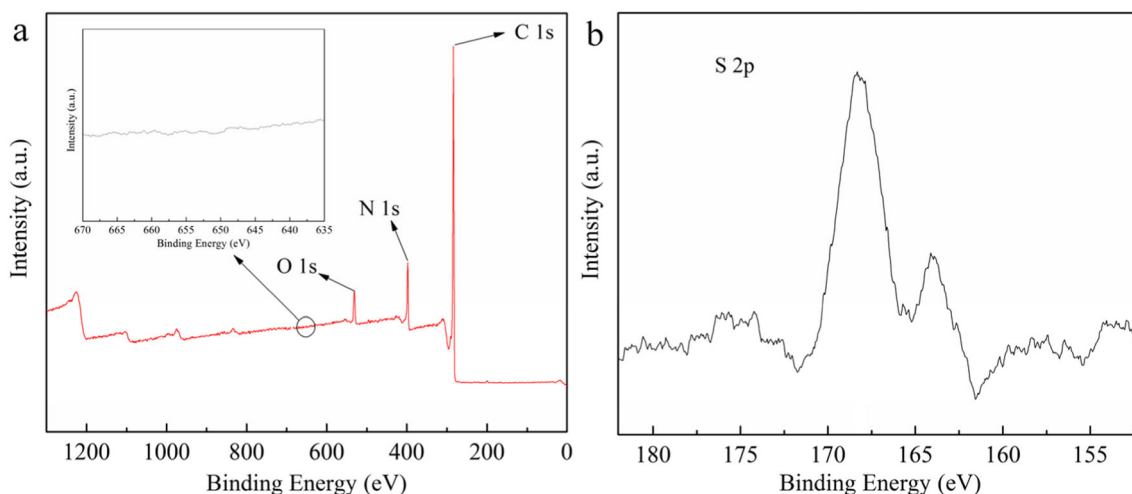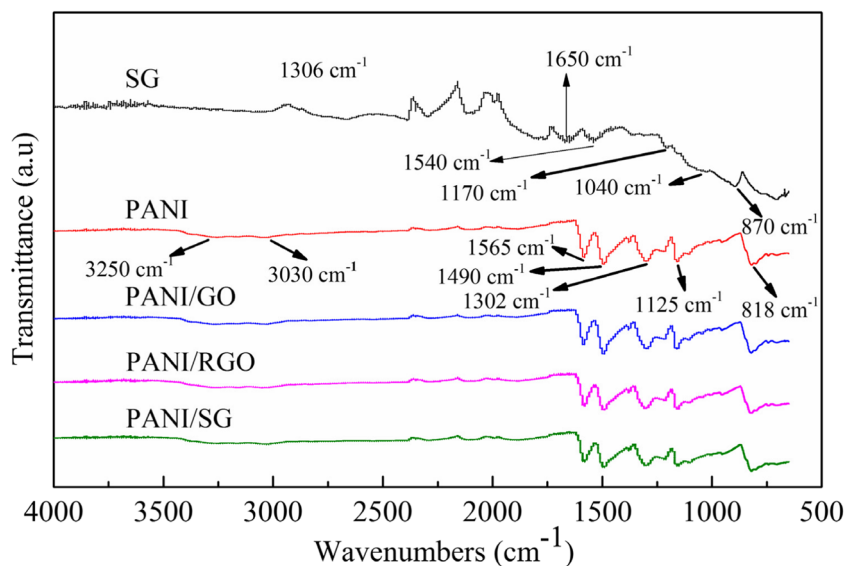

Fig. 2 **a** XPS spectrum of PANI/SG sample. **b** S 2p XPS spectrum of PANI/SG sample

Furthermore, the typical absorption bands of GO are not obvious because of its mass fraction in the composites is only 2%.

The morphologies of GO, RGO, and SG were visually examined by FESEM. The morphology and microconstruction of the samples are shown in Fig. 4. Without exception, a layered structure has been observed in FESEM images of GO, RGO, and SG, which derives from the heaping of the graphene nanosheets on account of the van der Waals force interaction. GO is composed of network structures and denser stacked layers of large number of graphene sheets, inheriting from graphite [43]. As shown in Fig. 4b, RGO displays a 3D interconnected porous network structure and the surface of RGO is crumpled and curved, exhibiting the prime characteristic of well-exfoliated thin sheets. The unique structures restrain the agglomeration of graphene layers and
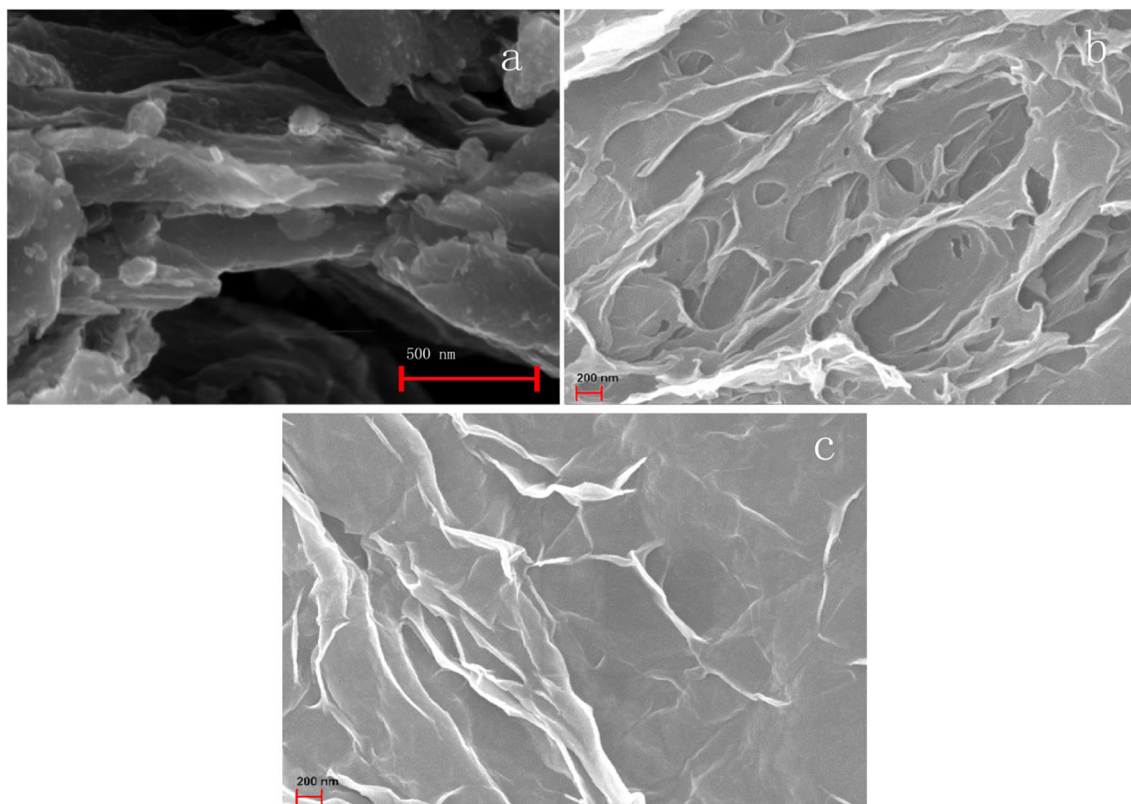

Fig. 4 FESEM images of **a** GO, **b** RGO, and **c** SG

make it possible for the pretty low density as well as the high specific surface area, which increase the active sites for the growth of PANI greatly. As shown in Fig. 4c, SG represents a rough surface with plenty of fluctuant waves, resulting from a conspicuous volume change during the reduction procedure.

As shown in Fig. 5a, the nanostructure of pure PANI was composed of nanofibers but in a denser clustered form compared with the PANI-based nanocomposites' hierarchical structure having rough surface is observed in Fig. 5b. In the FESEM micrographs of PANI/RGO composite, it is obvious to see the polymers are grown in the surface and galleries of RGO so that graphene served as soft template to suppress the aggregated and agglomerated phenomenons of PANI. The FESEM image of PANI/SG

(Fig. 5d) shows three-dimensional network morphology, and PANI nanofibers or nanoparticles with smaller diameters display the non-uniform growth on sulfonated graphene. In the meantime, the PANI acts as the spacer stuck in the middle of SGs enormously realizes the effective segregation of sulfonated graphene, giving rise to a reinforced active sites for heterogeneous plating polyaniline. The TEM image (Fig. 5e) further affirms the conjugate constructions of the polyaniline nanosphere and sulfonated graphene. Typical redispersed few-layer structure of SG is clearly shown in the TEM image and TEM image shows that the SG sheets are surrounded with PANI and mainly grown on the surface of the SG sheets which indicated that the PANI/SG nanocomposites were
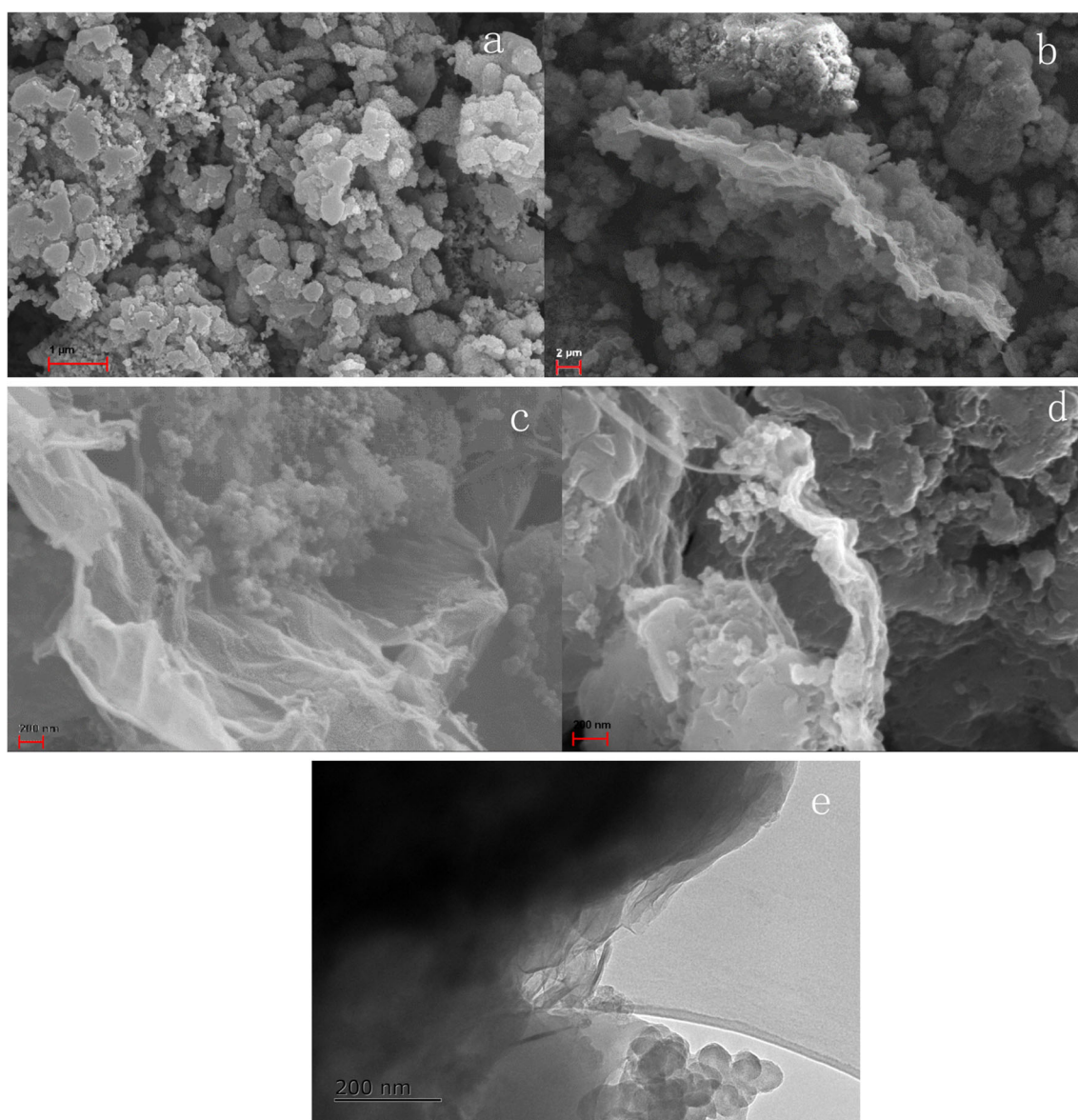

Fig. 5 FESEM images of **a** PANI, **b** PANI/GO, **c** PANI/RGO, and **d** PANI/SG. **e** TEM image of PANI/SG

successfully synthesized while sometimes PANI does not cover the whole surface area of sulfonated graphene [43].

Electrochemical properties

Some effective approaches such as CV, GCD, and EIS are used to estimate electrochemical properties of the obtained samples. Figure 6a shows the typical CV curves of the PANI and PANI-containing composites. The CV curves show two obvious redox peaks for each oxidation and reduction process for electrode materials, which can be attributed to various redox states of PANI. To be specific, it is the leucoemeraldine/emeraldine and emeraldine/pernigraniline structural transitions that imply good pseudocapacitance characteristics [48]. There are several feeble peaks around 0–0.2 V, which represent the by-products and intermediates of the hydroquinone/benzoquinone redox reaction. As can be seen, PANI/SG has a distinct edge in CV loop area over other materials, signifying higher specific capacitance and preferable electrochemical performance [49]. Enhanced capacitive be-

havior is due to the presence of the SG in the PANI matrix that provides high surface area for the polymerization of PANI and PANI can also enhance the electrode–electrolyte interface area, which facilitates rapid electrolyte ion transportation in the electrode matrix during charge–discharge processes [50].

Figure 6b shows the charge/discharge curves at the current density of 1 A/g. The specific capacitance of the samples is calculated from the galvanostatic charging/discharging curves according to Eq. (4) [51]:

$$C_{\mathrm{m}} = (I\Delta t)/(\Delta V m) \tag{4}$$

In which, C_{m} is the specific capacitance (F/g), I is the applied discharge current (A), Δt is the time of a discharge cycle (s), ΔV is discharge potential range, which is 0.8 V in this work, and m is the mass of the active materials of the electrode (g). The specific capacitance (C_{m}) of PANI, PANI/GO, PANI/RGO, and PANI/SG electrodes is 550.4, 700.6, 750.6, and
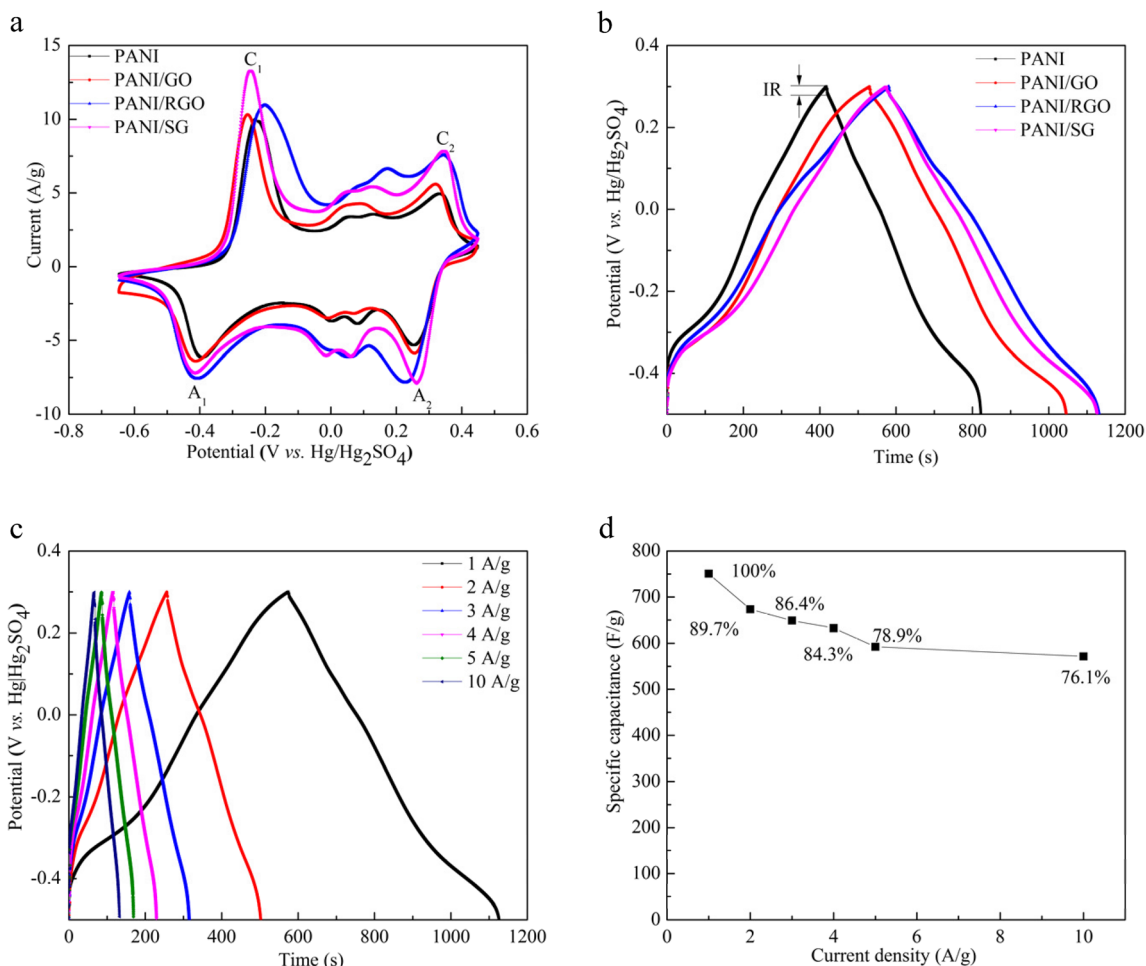

Fig. 6 **a** CV curves of PANI, PANI/GO, PANI/RGO, and PANI/SG at 5 mV/s. **b** GCD curves for PANI, PANI/GO, PANI/RGO, and PANI/SG nanocomposites at the current density of 1 A/g. **c** GCD curves of PANI/ SG electrode at different current densities. **d** Specific capacitance of PANI/SG composite calculated from the different current densities

752.3 F/g, respectively. Similar to the CV measurements, PANI/SG nanocomposite shows longer discharge time and more capacitance than those of pristine PANI and PANI/GO, obviously. The outcomes precisely prove that chemical bond facilitated the capacitive performance of the PANI/SG nanocomposite to a great extent. The high specific capacitance of PANI/SG is attributed to the unique nanostructure of PANI on the surface of sulfonated graphene, which benefits the diffusion of ions from the bulky electrolyte to the surface of the PANI to enhance the utilization of active materials as well as shortening the ionic-diffusion path and charge-transport distance in the hybrids [52]. Furthermore, because pure PANI itself has high internal resistance, the "IR drop" of PANI is much higher than that of PANI-based composites. Lower internal resistance of the electrode material is conducive to performing its rate performance at high current densities in supercapacitors.

The gravimetric specific capacitances of the electrode at different discharge current densities are shown in Fig. 6c. The curves show a deviation from perfect linearity, which is the obvious characteristic of polyaniline pseudocapacitors [53]. Moreover, the shape of all GCD curves is nearly symmetric with increasing the current density from 1 to 10 A/g. The specific capacitances of the electrode at different discharge current densities are summarized in Fig. 6d for obvious comparison. The gravimetric specific capacitances of the PANI/SG material were calculated to be about 752.3 $F \cdot g^{-1}$ ($1 \ A \cdot g^{-1}$) and 674.8 $F \cdot g^{-1}$ ($2 \ A \cdot g^{-1}$), respectively; the capacitive retention is 89.7%. Even though the current density reaches up to 10 A/g, 76.1% of the specific capacitance (572.2 F/g) is retained, which demonstrate the electrode material has a good flexibility to high current and excellent rate capability on account for the benefits of unique structured electrode. Furthermore, the prominent rate performance can be due to the high electroconductibility of SG as a support accelerated the transfer of charges during the charge–discharge process [52]. C_m decreases with increase of current density in that ions at lower currents have enough time to spread into the inner of the active substance, but at high currents, the electrolyte ions cannot penetrate into the most of the material under the relaxation effect.

For a detailed study of the nanocomposites, EIS was carried out in the frequency range from 100 kHz to 10 mHz to probe into electrode dynamics. Figure 7 represents the Nyquist plots obtained at open circuit potential for the PANI-based electrodes. As shown in Fig. 7, the lines of the PANI-based nanocomposites at the low frequency region are steep, indicating the good capacitive behavior and low resistance [54]. And the plot of the PANI/SG electrode exhibits the largest slop, demonstrating almost ideal capacitive behavior and the highest conductivity or lowest internal resistance, including polarization impedance. The semicircle in the high frequency region of the Nyquist plot is characteristic of a
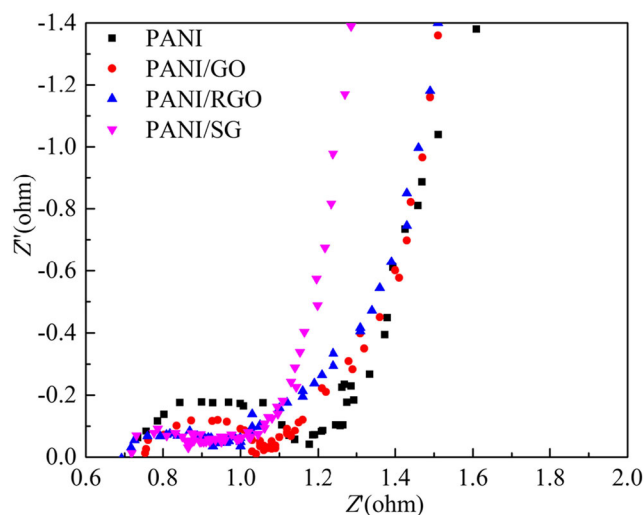

Fig. 7 Nyquist plots of pure PANI, PANI/GO, PANI/RGO, and PANI/SG composites

single time constant circuit [55]. The diameter of the semicircle stands for the charge transfer resistance (R_{ct}), which is related to the difficulty of the electric charge's directional migration between current collector, active substance, and electrolyte. At a high frequency, the smallest arc can be observed for PANI/SG nanocomposite indicating the lower resistance of PANI/SG compared to other materials, which ascribes to the reasonable nanostructure of PANI/SG and the high conductivity of SGs because of the disappearance of oxygen containing functional groups. The smaller R_{ct} is favorable for charge transfer through the hybrids, resulting in larger capacitance. The real-axis intercept at high frequency is equivalent to the irretrievable resistance of the electrolyte solution, which is also referred to as R_s. R_s of PANI, PANI/GO, PANI/RGO, and PANI/SG are similar because we assembled the three-electrode cell according to the same fabrication process with the identical electrolyte and current collector, implying the small electrolyte resistance and declaring the fabrication process of the electrode being reasonable.

Fabrication and characterization of ASC

In order to take full advantage of the large pseudocapacitance of the polyaniline material and the fast charge transfer ability of activated carbon (AC), we made them negative and positive electrodes respectively to fabricate asymmetric supercapacitors (ASCs) for more detailed performance testing. It must be considered that an ASC should keep charges at positive (q+) and negative (q−) balance (q+ = q−), and q could be estimated by the following equation [56].

$$q = mC_m \Delta V \tag{5}$$

The mass ratio (m_2/m_1) can be determined from the charge balanced equation, $q+ = q-$, as follows:

$$\frac{m_2}{m_1} = (\Delta V_1 \times C_{m1})/(\Delta V_2 \times C_{m2}) \qquad (6)$$

After calculation, the optimum mass ratio between the positive and negative electrodes ought to be about 2.6 in the present ASC device. The electrochemical properties of ASCs assembled with PANI/SG were evaluated by using CV, GCD, EIS, and cyclic stability test. CV curves of the PANI/SG//AC ASC and other as-fabricated ASC devices were characterized at various operating potentials varying from − 0.6–0.2 to − 0.6–0.8 V that are explicitly showed in Fig. 8a. Not surprisingly, there are no polarization phenomena appearing on the CV curves of the ASC even the voltage window was extended to 1.4 V, indicating that our assembled ASC was proper and stable. It is obvious to see that a pair of redox peaks appeared on the CV curves at around 0 or 0.4 V, reflecting the psuedocapacitive behavior of the conducting

polymer. Moreover, we performed the CV test at different scan rates within − 0.6–0.8 V cell voltage for the PANI/SG//AC ASC, and the test curves are depicted in Fig. 8b. As we can see, with the increase of scan rates, all the curves keep a relatively regular shape and the peak current intensities also increase obviously, showing the great reversible redox ability and excellent rate capability desirable for supercapcitors [57].

The galvanostatic charge–discharge curves of the PANI/SG//AC ASC at a current density of 0.5 A g^{-1} are depicted in Fig. 8c. Owing to the excellent capacitive performance of PANI/SG//AC ASC, curves display superior symmetry at a cell voltage as high as 1.4 V. It is found that the specific capacitance of ASC calculated based on the total mass of both active electrode materials reaches 90.9 F/g at a current density of 0.5 A/g. According to Fig. 8d, the maximum specific capacitance for the ASC reaches 128.4 F/g at a current density of 0.1 A/g. As the current density increases from 0.1 to 2 A/g, GCD curves still display superior symmetry, demonstrating the ideal capacitive characteristic again. The specific
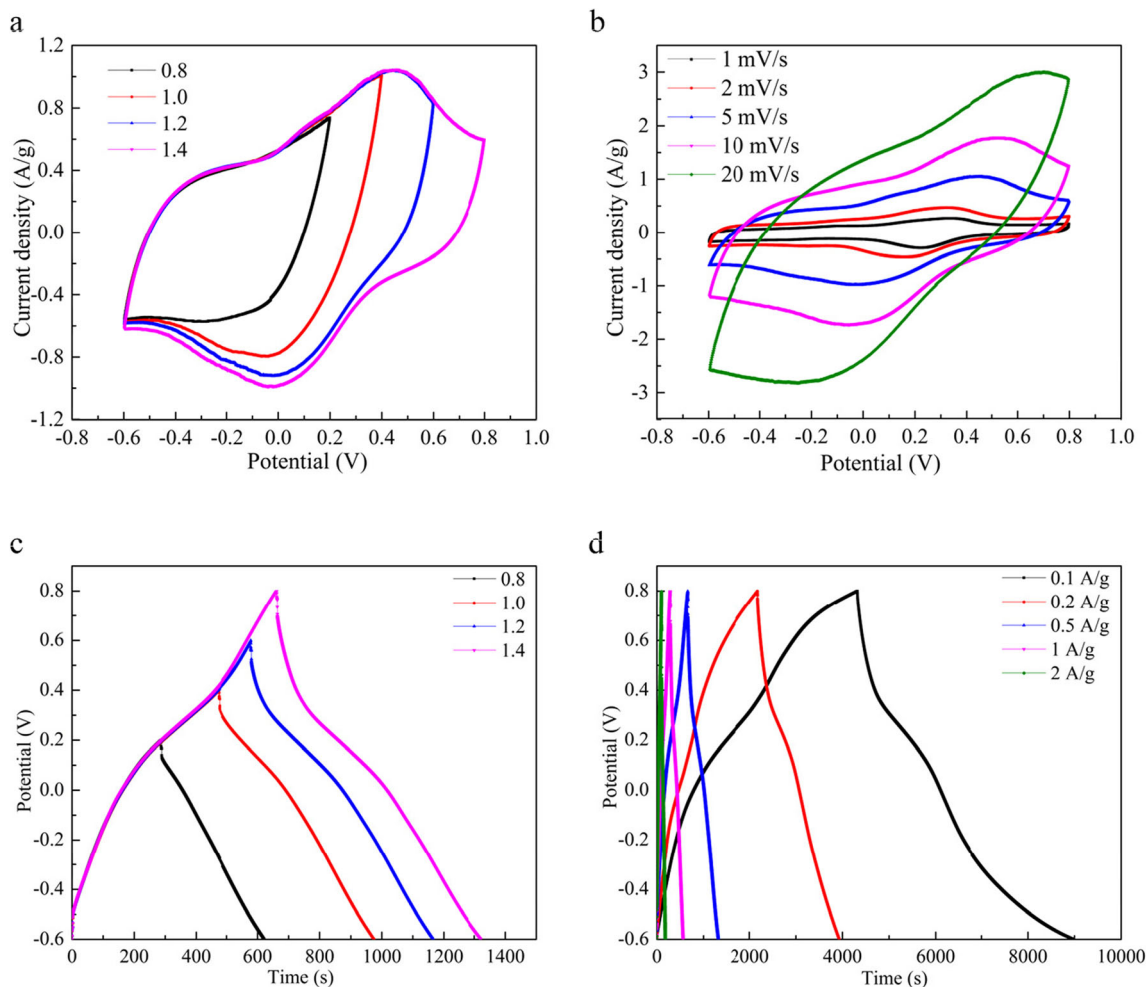

Fig. 8 a CV curves of PANI/SG//AC ASC at various voltage windows ranging from 0.8 to 1.4 V. b CV curves of PANI/SG//AC ASC at different scan rates of 1, 2, 5, 10, and 20 mV·s^{-1}. c Galvanostatic charge–discharge curves at a current density of 0.5 A·g^{-1}. d Galvanostatic charge/discharge curves of ASC for the calculation of gravimetric specific capacitance at different current densities
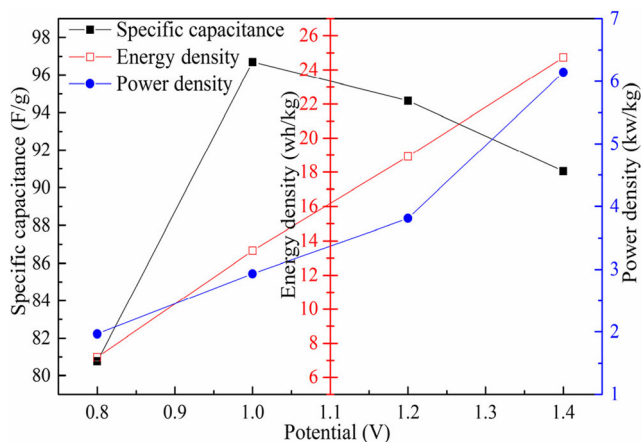
Fig. 9 A comparison of specific capacitances, energy densities, and power densities of ASC at different voltage windows at a current density of 0.5 A·g^{-1}

Fig. 11 Ragone plot of the asymmetric device based on PANI/SG and AC electrodes

capacitance for the ASC decreases with the current density increasing, which is ascribed to the incomplete redox reaction resulted from the insufficient time and the poor connection in the electrochemical system with the increased current [31]. Specific capacitances, energy densities, and power densities of the ASC device with an increase of the cell voltage are depicted on Fig. 9.

Considering the practical application, cycling stability is a vital characteristic for evaluating the performance of energy storage devices, which was confirmed by repeating the GCD test within − 0.6–0.8 V at a current density of 1 A·g^{-1} (Fig. 10). On account of the degradation was derived from the expansion and shrinkage of PANI over repeated charging/discharging processes, the capacitance retention of PANI after 5000 cycles is only 71.5% of its initial capacitance. After 1000 cycles, specific capacitance values of the ASC-based PANI/SG//AC still reserve about 94.6% relative to the initial figure while capacitive
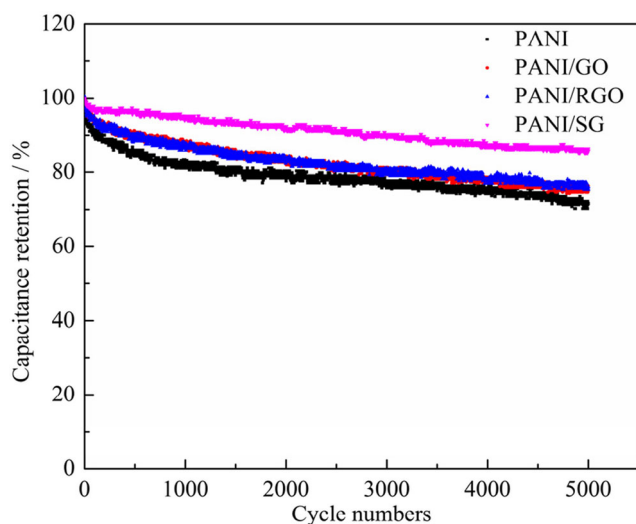
retention is about 85.9% after 5000 cycles, suggesting remarkable cycling stability. The improved cycling performance results from synergistic effects of PANI and SG backbone [58]. Sulfonated graphene can restrain the volumetric change of PANI to improve the charge transfer kinetics; in the meantime, the PANI arrays uniformly on the SGs displayed relaxation of the surface tension, which enabled the decrease of structural damage to come true during the long-range charge–discharge processes [49].

Next, Fig. 11 depicts the relationship between the energy density and power density of the asymmetric supercapacitor at different current densities. Ragone plots are one of the effective ways to appraise the capacitive performance of asymmetric supercapacitors. The average power density still remains about 6.1 kW·kg^{-1} even at a high energy density of 23 Wh·kg^{-1}, proving the ASC was receivable. Most of all, the energy density of the PANI/SG//AC ASC is markedly higher than those of PANI/graphene composite-based supercapacitor (18.8 Wh·kg^{-1} at 0.1 kW·kg^{-1}) [59] and layered PPy/graphene film-based supercapacitor (20.6 Wh·kg^{-1} at 1.28 kW·kg^{-1}) [60].

Conclusion

In summary, covalently bonded PANI/SG nanocomposite was synthesized successfully by functionalizing RGO with sulfanilic acid meanwhile applying it as the template in situ chemical polymerization of aniline. The as-obtained PANI/SG composite acquired outstanding electrochemical properties, including a high gravimetric specific capacitance, up to 750.6 F·g^{-1} at 1.0 A·g^{-1} and a good rate property (76.1% capacitance retention at 10 A·g^{-1}) in the three-electrode test. The assembled asymmetric cell based on this material as the negative electrode and pre-treated activated carbon as the positive electrode can be cycled reversibly at a cell voltage of 1.4 V in a 2 M HClO$_4$ aqueous electrolyte, delivering both a high gravimetric energy density (23 Wh·kg^{-1} at a power

Fig. 10 Charge–discharge cyclic stability of PANI//AC, PANI/GO//AC, PANI/RGO//AC, and PANI/SG//AC at 1 A·g^{-1} current density of the asymmetric device

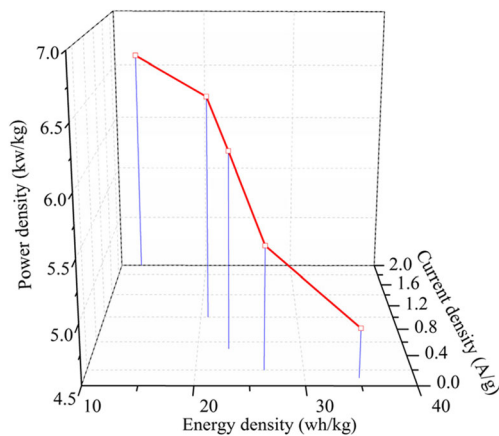density of 6.1 kW·kg^{-1}) and a prominent electrochemical stability (85.9% capacity retention after 5000 cycles at 1.0 A·g^{-1}). These inspiring consequences can usher in the feasibility of PANI-based ASC suitable for the increasing requirements on the high-performance electrochemical capacitor and other electronic systems.

References

1. Fominykh K, Feckl JM, Sicklinger J, Döblinger M, Böcklein S, Ziegler J, Peter L, Rathousky J, Scheidt E, Bein T, Fattakhova-Rohlfing D (2014) Ultrasmall dispersible crystalline nickel oxide nanoparticles as high-performance catalysts for electrochemical water splitting. Adv Funct Mater 24(21):3123–3129

2. Iqbal S, Bahadur A, Saeed A, Zhou K, Shoaib M, Waqas M (2017) Electrochemical performance of 2D polyaniline anchored CuS/graphene nano-active composite as anode material for lithium-ion battery. J Colloid Interface Sci 502:16–23

3. Dubal DP, Ayyad O, Ruiz V, Romero PG (2015) Hybrid energy storage: the merging of battery and supercapacitor chemistries. Chem Soc Rev 46:1777–1790

4. Yang Z, Zhang J, Kintner-Meyer MC, Lu X, Choi D, Lemmon JP, Liu J (2011) Electrochemical energy storage for green grid. Chem Rev 111(5):3577–3613

5. Zhai Y, Dou Y, Zhao D, Fulvio PF, Mayes RT, Dai S (2011) Carbon materials for chemical capacitive energy storage. Adv Mater 23(42):4828–4850

6. Goodenough JB (2013) Evolution of strategies for modern rechargeable batteries. Acc Chem Res 46(5):1053–1061

7. Béguin F, Presser V, Balducci A, Frackowiak E (2014) Carbons and electrolytes for advanced supercapacitors. Adv Mater 26(14):2219–2251

8. Snook GA, Kao P, Best AS (2011) Conducting-polymer-based supercapacitor devices and electrodes. J Power Sources 196(1):1–12

9. Al-Enizi AM, Elzatahry AA, Abdullah AM, AlMaadeed MA, Wang J, Zhao D, Al-Deyab S (2014) Synthesis and electrochemical properties of nickel oxide/carbon nanofiber composites. Carbon 71:276–283

10. Kim TY, Jung G, Yoo S, Suh KS, Ruoff RS (2013) Activated graphene-based carbons as supercapacitor electrodes with macro- and mesopores. ACS Nano 7(8):6899–6905

11. Kim M, Kim Y, Lee KM, Jeong SY, Lee E, Baeck SH, Shim SE (2016) Electrochemical improvement due to alignment of carbon nanofibers fabricated by electrospinning as an electrode for supercapacitor. Carbon 99:607–618

12. Yan J, Wang Q, Wei T, Fan Z (2014) Recent advances in design and fabrication of electrochemical supercapacitors with high energy densities. Adv Energy Mater 4:157–164

13. Huang H, Gan M, Ma L, Yu L, Hu H, Yang F, Li Y, Ge C (2015) Fabrication of polyaniline/graphene/titania nanotube arrays nanocomposite and their application in supercapacitors. J Alloys Compd 630:214–221

14. Zhang YQ, Xia XH, Tu JP, Mai YJ, Shi SJ, Wang XL, Gu CD (2012) Self-assembled synthesis of hierarchically porous NiO film and its application for electrochemical capacitors. J Power Sources 199:413–417

15. Wang L, Yu J, Dong X, Li X, Xie Y, Chen S, Li P, Hou H, Song Y (2016) Three-dimensional macroporous carbon/Fe$_3$O$_4$-doped porous carbon nanorods for high-performance supercapacitor. ACS Sustain Chem Eng 4(3):1531–1537

16. Wang Y, Xu S, Liu W, Cheng H, Chen S, Liu X, Liu J, Tai Q, Hu C (2017) Facile fabrication of urchin-like polyaniline microspheres for electrochemical energy storage. Electrochim Acta 254:25–35

17. Gao S, Zang P, Dang L, Xu H, Shi F, Liu Z, Lei Z (2016) Extraordinarily high-rate capability of polyaniline nanorod arrays on graphene nanomesh. J Power Sources 304:111–118

18. Goubard-Bretesché N, Crosnier O, Favier F, Brousse T (2016) Improving the volumetric energy density of supercapacitors. Electrochim Acta 206:458–463

19. Zhu D, Cheng K, Wang Y, Sun D, Gan L, Chen T, Jiang J, Liu M (2017) Nitrogen-doped porous carbons with nanofiber-like structure derived from poly (aniline-co-p-phenylenediamine) for supercapacitors. Electrochim Acta 224:17–24

20. Liu M, Shi M, Lu W, Zhu D, Li L, Gan L (2017) Core-shell reduced graphene oxide/MnOx@carbon hollow nanospheres for high performance supercapacitor electrodes. Chem Eng J 313:518–526

21. Candelaria SL, Shao Y, Zhou W, Li X, Xiao J, Zhang J, Wang Y, Liu J, Li J, Cao G (2012) Nanostructured carbon for energy storage and conversion. Nano Energy 1(2):195–220

22. Wu ZS, Zhou G, Yin LC, Ren W, Li F, Cheng H (2012) Graphene/metal oxide composite electrode materials for energy storage. Nano Energy 1(1):107–131

23. Xia X, Tu J, Zhang Y, Wang X, Gu C, Zhao XB, Fan HJ (2012) High-quality metal oxide core/shell nanowire arrays on conductive substrates for electrochemical energy storage. ACS Nano 6(6):5531–5538

24. Tong Z, Yang Y, Wang J, Zhao J, Su B, Li Y (2014) Layered polyaniline/graphene film from sandwich-structured polyaniline/graphene/polyaniline nanosheets for high-performance pseudosupercapacitors. J Mater Chem A 2(13):4642–4651

25. Wang H, Hao Q, Yang X, Lu L, Wang X (2010) A nanostructured graphene/polyaniline hybrid material for supercapacitors. Nanoscale 2(10):2164–2170

26. Li D, Huang J, Kaner RB (2009) Polyaniline nanofibers: a unique polymer nanostructure for versatile applications. Acc Chem Res 42(1):135–145

27. Hu H, Liu S, Hanif M, Chen S, Hou H (2014) Three-dimensional cross-linked carbon network wrapped with ordered polyaniline nanowires for high-performance pseudo-supercapacitors. J Power Sources 268:451–458

28. Ramkumar R, Sundaram MM (2016) Electrochemical synthesis of polyaniline cross-linked NiMoO$_4$ nanofibre dendrites for energy storage devices. New J Chem 40(9):7456–7464

29. Chang CM, Hu ZH, Lee TY, Huang Y, Ji W, Liu W, Yeh J, Wei Y (2016) Biotemplated hierarchical polyaniline composite electrodes with high performance for flexible supercapacitors. J Mater Chem A 4(23):9133–9145

30. Liu P, Han JJ, Jiang LF, Li ZY, Cheng JN (2017) Polyaniline/multi-walled carbon nanotubes composite with core-shell structures as a cathode material for rechargeable lithium-polymer cells. Appl Surf Sci 400:446–452

31. Male U, Modigunta JKR (2017) Design and synthesis of polyaniline-grafted reduced graphene oxide via azobenzene pendants for high-performance supercapacitors. Polymer 110:242–249

32. Raccichini R, Varzi A, Passerini S, Scrosati B (2015) The role of graphene for electrochemical energy storage. Nat Mater 14(3):271–279

33. Golikand AN, Bagherzadeh M, Shirazi Z (2017) Evaluation of the polyaniline based nanocomposite modified with graphene nanosheet, carbon nanotube, and Pt nanoparticle as a material for supercapacitor. Electrochim Acta 247:116–124

34. Ashok KN, Baek JB (2014) Electrochemical supercapacitors from conducting polyaniline-graphene platforms. Chem Commun 50(48):6298–6308

35. Wang L, Lu X, Lei S, Song Y (2014) Graphene-based polyaniline nanocomposites: preparation, properties and applications. J Mater Chem A 2(13):4491–4509

36. Ma B, Zhou X, Bao H, Li X, Wang G (2012) Hierarchical composites of sulfonated graphene-supported vertically aligned polyaniline nanorods for high-performance supercapacitors. J Power Sources 215:36–42

37. Fan T, Tong S, Zeng W, Niu Q, Liu Y, Kao C, Liu J, Huang W, Min Y, Epstein AJ (2015) Self-assembling sulfonated graphene/polyaniline nanocomposite paper for high performance supercapacitor. Synth Met 199:79–86

38. Hummers JW, Offeman RE (1958) Preparation of graphitic oxide. J Am Chem Soc 80(6):1339–1339

39. Bagherzadeh M, Heydari M (2013) Electrochemical detection of dopamine based on pre-concentration by graphene nanosheets. Analyst 138(20):6044–6051

40. Zhang LL, Zhao X, Stoller MD, Zhu Y, Ji H, Murali S, Wu Y, Perales S, Clevenger B, Ruoff RS (2012) Highly conductive and porous activated reduced graphene oxide films for high-power supercapacitors. Nano Lett 12(4):1806–1812

41. Fu XB, Feng JY, Wang H, Ng KM (2010) Fast synthesis and formation mechanism of γ-MnO2 hollow nanospheres for aerobic oxidation of alcohols. Mater Res Bull 45(9):1218–1223

42. Zhang J, Shu D, Zhang TR, Chen HY, Zhao HM, Wang YS, Sun ZJ, Tang SQ, Fang XM, Cao XF (2012) Capacitive properties of PANI/MnO2 synthesized via simultaneous-oxidation route. J Alloys Compd 532:1–9

43. Htut KZ, Kim M, Lee E, Lee G, Baeck SH, Shim SE (2017) Biodegradable polymer-modified graphene/polyaniline electrodes for supercapacitors. Synth Met 227:61–70

44. Hao Q, Wang H, Yang X, Lu L, Wang X (2011) Morphology-controlled fabrication of sulfonated graphene/polyaniline nanocomposites by liquid/liquid interfacial polymerization and investigation of their electrochemical properties. Nano Res 4(4):323–333

45. Yuan WH, Gu YJ, Li BQ, Li L (2012) Synthesis and characterization of sulfonated graphene and conducting films. J Inorg Mater 27:1271–1276

46. Pan C, Gu H, Dong L (2016) Synthesis and electrochemical performance of polyaniline@MnO2/graphene ternary composites for electrochemical supercapacitors. J Power Sources 303:175–181

47. Bandyopadhyay P, Kuila T, Balamurugan J, Nguyen TT, Kim NH, Lee JH (2017) Facile synthesis of novel sulfonated polyaniline functionalized graphene using m-aminobenzene sulfonic acid for asymmetric supercapacitor application. Chem Eng J 308:1174–1184

48. Yu P, Li Y, Zhao X, Wu L, Zhang Q (2014) Graphene-wrapped polyaniline nanowire arrays on nitrogen-doped carbon fabric as novel flexible hybrid electrode materials for high-performance supercapacitor. Langmuir 30(18):5306–5313

49. Jin LN, Shao F, Jin C, Zhang J, Liu P, Guo M, Bian S (2017) High-performance textile supercapacitor electrode materials enhanced with three-dimensional carbon nanotubes/graphene conductive network and in situ polymerized polyaniline. Electrochim Acta 249:387–394

50. Hao M, Chen Y, Xiong WL, Zhang L, Wu LY, Fu Y, Mei T, Wang JY, Li JH, Wang XB (2016) Coherent polyaniline/graphene oxides/multi-walled carbon nanotubes ternary composites for asymmetric supercapacitors. Electrochim Acta 191:165–172

51. Stoller MD, Ruoff RS (2010) Methods and best practices for determining an electrode material's performance for ultracapacitors. Energy Environ Sci 3(9):1294–1301

52. Zhang Z, Xiao F, Xiao J, Wang S (2015) Functionalized carbonaceous fibers for high performance flexible all-solid-state asymmetric supercapacitors. J Mater Chem A 3(22):11817–11823

53. Khosrozadeh A, Xing M, Wang Q (2015) A high-capacitance solid-state supercapacitor based on free-standing film of polyaniline and carbon particles. Appl Energy 153:87–93

54. Tran VC, Nguyen VH, Nguyen TT, Lee JH, Huynh DC, Shim J (2016) Polyaniline and multi-walled carbon nanotube-intercalated graphene aerogel and its electrochemical properties. Synth Met 215:150–157

55. Liu Y, Ma Y, Guang S, Xu H, Su X (2014) Facile fabrication of three-dimensional highly ordered structural polyaniline–graphene bulk hybrid materials for high performance supercapacitor electrodes. J Mater Chem A 2(3):813–823

56. Yan J, Fan Z, Sun W, Ning G, Wei T, Zhang Q, Zhang R, Zhi L, Wei F (2012) Advanced asymmetric supercapacitors based on Ni(OH)2/graphene and porous graphene electrodes with high energy density. Adv Funct Mater 22(12):2632–2641

57. Yu H, Ge X, Bulin C, Xing R, Li R, Xin G, Zhang B (2017) Facile fabrication and energy storage analysis of graphene/PANI paper electrodes for supercapacitor application. Electrochim Acta 253:239–247

58. Bulin C, Yu H, Ge X, Xin G, Xing R, Li R, Zhang B (2017) Preparation and supercapacitor performance of functionalized graphene aerogel loaded with polyaniline as a freestanding electrode. J Mater Sci 52(10):5871–5881

59. Wu Q, Xu Y, Yao Z, Liu A, Shi G (2010) Supercapacitors based on flexible graphene/polyaniline nanofiber composite films. ACS Nano 4(4):1963–1970

60. Li S, Zhao C, Shu K, Wang C, Guo Z, Wallace GG, Liu H (2014) Mechanically strong high performance layered polypyrrole nano fibre/graphene film for flexible solid state supercapacitor. Carbon 79:554–562